



HAL
open science

Insights into Triazolylidene Ligands Behaviour at a Di-Iron Site Related to [FeFe]-Hydrogenases

Andrea Mele, Federica Arrigoni, Catherine Elleouet, François Pétillon, Philippe Schollhammer, Giuseppe Zampella

► **To cite this version:**

Andrea Mele, Federica Arrigoni, Catherine Elleouet, François Pétillon, Philippe Schollhammer, et al.. Insights into Triazolylidene Ligands Behaviour at a Di-Iron Site Related to [FeFe]-Hydrogenases. *Molecules*, 2022, 27 (15), pp.4700. <10.3390/molecules27154700>. <hal-03917886>

HAL Id: hal-03917886

<https://hal.science/hal-03917886v1>

Submitted on 11 Jan 2024

HAL is a multi-disciplinary open access archive for the deposit and dissemination of scientific research documents, whether they are published or not. The documents may come from teaching and research institutions in France or abroad, or from public or private research centers.


L'archive ouverte pluridisciplinaire **HAL**, est destinée au dépôt et à la diffusion de documents scientifiques de niveau recherche, publiés ou non, émanant des établissements d'enseignement et de recherche français ou étrangers, des laboratoires publics ou privés.



HAL Authorization

Article

Insights into Triazolylidene Ligands Behaviour at a Di-Iron Site Related to [FeFe]-Hydrogenases

Andrea Mele ¹, Federica Arrigoni ^{2,*}, Catherine Elleouet ^{1,*}, François Y. Pétilion ¹, Philippe Schollhammer ^{1,*} 
and Giuseppe Zampella ^{2,*}

¹ Laboratoire de Chimie, Electrochimie Moléculaire et Chimie Analytique, UMR 6521 CNRS-Université de Bretagne Occidentale, CS 93837—6 Avenue Le Gorgeu, CEDEX 3, 29238 Brest, France; chemandmele@gmail.com (A.M.); francois.petillon@univ-brest.fr (F.Y.P.)

² Department of Biotechnology and Bioscience, University of Milano-Bicocca Piazza della Scienza 2, 20126 Milan, Italy

* Correspondence: federica.arrigoni@unimib.it (F.A.); catherine.elleouet@univ-brest.fr (C.E.); philippe.schollhammer@univ-brest.fr (P.S.); giuseppe.zampella@unimib.it (G.Z.)

Abstract: The behaviour of triazolylidene ligands coordinated at a {Fe₂(CO)₅(μ-dithiolate)} core related to the active site of [FeFe]-hydrogenases have been considered to determine whether such carbenes may act as redox electron-reservoirs, with innocent or non-innocent properties. A novel complex featuring a mesoionic carbene (MIC) [Fe₂(CO)₅(Pmpt)(μ-pdt)] (**1**; Pmpt = 1-phenyl-3-methyl-4-phenyl-1,2,3-triazol-5-ylidene; pdt = propanedithiolate) was synthesized and characterized by IR, ¹H, ¹³C{¹H} NMR spectroscopies, elemental analyses, X-ray diffraction, and cyclic voltammetry. Comparison with the spectroscopic characteristics of its analogue [Fe₂(CO)₅(Pmbt)(μ-pdt)] (**2**; Pmbt = 1-phenyl-3-methyl-4-butyl-1,2,3-triazol-5-ylidene) showed the effect of the replacement of a n-butyl by a phenyl group in the 1,2,3-triazole heterocycle. A DFT study was performed to rationalize the electronic behaviour of **1**, **2** upon the transfer of two electrons and showed that such carbenes do not behave as redox ligands. With highly perfluorinated carbenes, electronic communication between the di-iron site and the triazole cycle is still limited, suggesting low redox properties of MIC ligands used in this study. Finally, although the catalytic performances of **2** towards proton reduction are weak, the protonation process after a two-electron reduction of **2** was examined by DFT and revealed that the protonation process is favoured by S-protonation but the stabilized diprotonated intermediate featuring a {Fe-H··H-S} interaction does not facilitate the release of H₂ and may explain low efficiency towards HER (Hydrogen Evolution Reaction).

Keywords: non-innocent ligand; redox ligand; mesoionic carbene; triazolylidene; DFT calculations; di-iron complexes; metal-sulfur; carbonyl; hydrogenases; bioinspiration



Citation: Mele, A.; Arrigoni, F.; Elleouet, C.; Pétilion, F.Y.; Schollhammer, P.; Zampella, G. Insights into Triazolylidene Ligands Behaviour at a Di-Iron Site Related to [FeFe]-Hydrogenases. *Molecules* **2022**, *27*, 4700. <https://doi.org/10.3390/molecules27154700>

Academic Editor: Artem L. Gushchin

Received: 1 July 2022

Accepted: 20 July 2022

Published: 22 July 2022

Publisher's Note: MDPI stays neutral with regard to jurisdictional claims in published maps and institutional affiliations.



Copyright: © 2022 by the authors. Licensee MDPI, Basel, Switzerland. This article is an open access article distributed under the terms and conditions of the Creative Commons Attribution (CC BY) license (<https://creativecommons.org/licenses/by/4.0/>).

1. Introduction

The catalytic site of [FeFe] hydrogenases (H-cluster) contains a di-iron sub-site with an azapropanedithiolate bridge and a cubane [Fe₄S₄] described as an electron sink, connected together by a sulfur atom of a cysteine [1–3]. The high activity of the H-cluster for the electrocatalytic H⁺/H₂ conversion relies on a fine electronic balance of charges and a well-suited geometry around the di-iron site that are controlled by electron and proton transfers mediated by the amine of the azadithiolate bridge, acting as a proton-relay, and the non-innocent redox [Fe₄S₄] cluster [4–8].

Carbonyl dithiolato bridged di-iron complexes have been, obviously, considered as the best candidates to mimic the H-cluster in reason of their strong structural resemblance and the high setting possibilities of their coordination sphere in order to modulate their redox and protic properties. For these reasons, such systems have aroused the interest of chemists for several years, allowing novel insights into the organometallic chemistry of di-iron complexes involving bimetallic and metal-ligand cooperativities [9–18]. In

this context, various redox ligands have been combined with such bio-inspired di-iron systems but very few of them display non-innocent behaviour and act as the [Fe₄S₄] cubane in the H-cluster [19–35]. A few years ago, the intriguing redox non-innocent behaviour of a N-heterocyclic carbene (NHC) was proposed for the two-electron reduction of the complex [Fe₂(CO)₅(IMes)(μ-pdt)] (IMes = 1,3-bis(2,4,6-trimethylphenyl)-imidazol-2-ylidene) through a simultaneous dual electron uptake by the di-iron site and the NHC ligand [30].

Among N-Heterocyclic Carbenes ligands, abnormal NHC ligands, also called mesoionic carbenes (MICs), are less reported in the literature [36–42]. Their canonical zwitterionic nature and the possibility of charge transfer upon bonding to the metal centre raise the question of their possible redox non-innocence and make them interesting for mimicking H-cluster charge transfers.

Recently, we reported the synthesis of the complex [Fe₂(CO)₅(Pmbt)(μ-pdt)] (**2**; Pmbt = 1-phenyl-3-methyl-4-butyl-1,2,3-triazol-5-ylidene; pdt = propanedithiolate) in order to investigate the potentially redox non-innocence of such triazolylidene carbenes at a di-iron site [43]. As expected, the ligand Pmbt was found to be a better donor than imidazol-2-ylidenes. The red-shift of the ν(CO) bands agreed with the evolution of the redox potentials compared to that of the hexacarbonyl complex. Unfortunately, the catalytic activity was non-existent or, at least, very inefficient.

The work presented herein is an extension of our previous results. An analogous complex [Fe₂(CO)₅(Pmpt)(μ-pdt)] (**1**; Pmpt = 1-phenyl-3-methyl-4-phenyl-1,2,3-triazol-5-ylidene) has been synthesized in which the aliphatic chain (butyl) of the MIC ligand (in **2**) has been replaced by an aromatic group (phenyl) in order to check the effect of such a modification on the electronic behaviour of the di-iron system. **1** was fully characterized and its electrochemical behaviour was examined by cyclic voltammetry.

DFT calculations were performed for both complexes with the aim to investigate the role of MIC ligands as redox active relay upon one- and two-electron transfers and to rationalize the influence of the modifications of the MIC ligands on the electronic communication between the di-iron core and the carbene. The protonation process after the transfer of two electrons was also considered.

2. Results and Discussion

2.1. Synthesis and Characterization

The preparation of **1** was realized according to the same protocol used for the synthesis of **2** from the precursor [Fe₂(CO)₆(μ-pdt)] in the presence of the Pmpt triazolium salt and a base (potassium tert-butoxide) (see Appendix A) (Figure S1) [43]. The IR spectrum of **1**, recorded in the carbonyl region, in CH₂Cl₂, is typical of monosubstituted complexes having a {Fe₂(CO)₅L} core, with four bands 2033(s), 1968(vs), 1945(sh), 1910(w) cm⁻¹ (Figure S2 in Supplementary Materials). Their comparison with those of **2** (2028(s), 1969(vs), 1950(sh), and 1907(w) cm⁻¹ [43]) shows that the replacement in the triazole carbene of the n-butyl chain with a more electron-withdrawing group, such as a phenyl, does not decrease significantly the σ-donor strength of this ligand. This accords with previous observations reported in the literature where the arrangement of the C- vs. N-bound substituents only plays a very slight role for tuning the electronic properties of the metal centre [44–46]. Furthermore, calculated ν(CO) values for **1**, **2** (Table S1 in Supplementary Materials) agree with such a trend. **1** has been characterized by ¹H and ¹³C{¹H} NMR spectroscopies in CD₂Cl₂ (Figures S3 and S4 in Supplementary Materials). These data are in accordance with the molecular structure of **1** described below and close to those of **2**. The ¹H NMR spectrum of **1** displays in the aromatic region (~7.6–7.7 ppm) the expected signals due to the two phenyls. The N-CH₃ group is detected at 3.90 ppm as a singlet and CH₂ of the pdt bridge are typically observed, as multiplets, at 1.78 (2H) and 1.63 (4H) ppm. In the ¹³C{¹H} NMR spectrum, the two signals at 216.4 (216.6 ppm for **2**) and 212.1 ppm (211.8 ppm for **2**) are attributed to the carbonyls of the {Fe(CO)₃-Fe(CO)₂} core. The peak at 173.3 ppm (171.2 ppm for **2**) is typical of the carbenic carbon of the triazolylidene ligand linked to

one iron atom. Other signals (see Appendix A) are assigned to the second carbon of the 1,2,3-triazole cycle, propanedithiolate, and N-Me groups.

Complex **1** was crystallized, as red single crystals, from slow evaporation of a solution hexane/THF (1:1) at $-30\text{ }^{\circ}\text{C}$ and its structure was determined by X-ray diffraction analysis (Figure 1 and Table S2 in Supplementary Materials). The Pmpt ligand lies in apical position, in contrast to Pmbt in **2**, which is in basal position, but similarly to the structure observed for other analogous imidazole-derived carbene complexes [30,31,33]. The apical position of the Pmpt ligand, that is observed experimentally for **1**, accords with the more stable forms determined by DFT calculations (apical isomer is more stable by 1.7 kcal/mol than the basal form). For **2**, the basal disposition of Pmbt has been confirmed as the most stable isomer, since the apical isomer is 2.7 kcal/mol higher in energy. This may reflect the different steric effects of the n-butyl and phenyl groups.

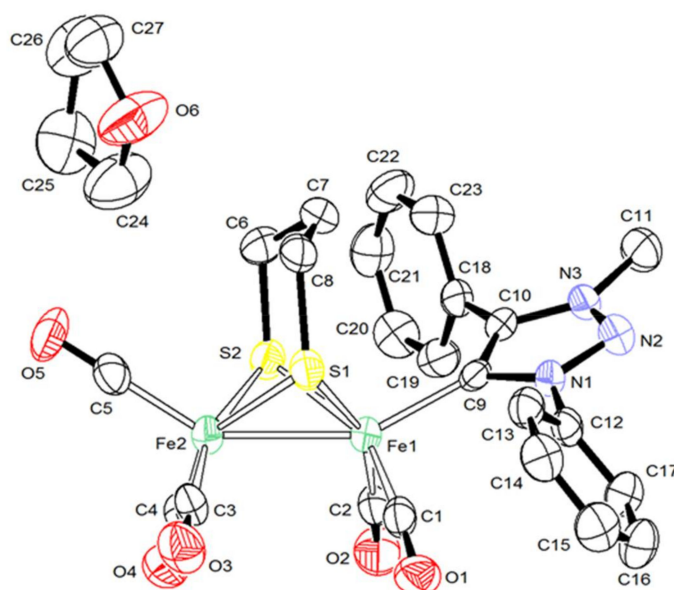


Figure 1. Ortep view (ellipsoids at 30% of probability level) of $1\cdot\text{C}_4\text{H}_8\text{O}$. Selected distances (\AA) and angles (deg): C9-Fe1, 1.980(5); Fe1-Fe2, 2.5275(11); S1-Fe1, 2.2781(16); S1-Fe2, 2.2726(15); S2-Fe2, 2.2704(17); S2-Fe1, 2.2707(15); C9-N1, 1.389(5); C9-C10, 1.409(7); C11-N3, 1.466(6); N1-N2, 1.343(5); N2-N3, 1.320(5); C10-N3, 1.366(6); C12-N1, 1.430(6); C1-O1, 1.166(6); C1-Fe1, 1.744(6); C2-O2, 1.135(6); C2-Fe1, 1.778(6); C3-O3, 1.137(6); C3-Fe2, 1.787(6); C4-O4, 1.158(6); C4-Fe2, 1.774(6); C5-O5, 1.154(6); C5-Fe2, 1.777(6); Fe1-S1-Fe2, 67.48(5); Fe2-S2-Fe1, 67.64(5); C5-Fe2-Fe1, 146.56(18); C9-Fe1-Fe2, 151.97(14); C1-Fe1-Fe2, 100.29(18); C2-Fe1-Fe2, 103.24(17); C3-Fe2-Fe1, 107.34(18); C4-Fe2-Fe1, 95.30(18); O1-C1-Fe1, 175.2(5); O2-C2-Fe1, 178.1(5); O3-C3-Fe2, 178.6(5); O4-C4-Fe2, 178.7(5); and O5-C5-Fe, 177.4(5).

The Fe-C_(MIC) distance (1.980(5) \AA) is very close to that observed in **2** (1.9839(19) \AA) and those reported for other NHC-monosubstituted di-iron complexes $[\text{Fe}_2(\text{CO})_5\text{L}(\mu\text{-pdt})]$ [33]. The Fe-Fe length (2.5275(11) \AA) is in the range of distances expected for single Fe(I)-Fe(I) bond in complexes $[\text{Fe}_2(\text{CO})_{6-x}\text{L}_x(\mu\text{-pdt})]$ [9]. A typical eclipsed geometry is observed around the two iron atoms which have a square pyramidal coordination geometry. The overall geometry of **1** is unexceptional and other X-ray data (distances and angles) will not be further described.

The electrochemical behaviour of **1** in $\text{CH}_2\text{Cl}_2\text{-}[\text{Bu}_4\text{N}][\text{PF}_6]$ 0.2 M is comparable to that of **2**. Indeed, **1** undergoes an irreversible reduction according to an ECE mechanism and a chemically reversible oxidation. The potential values are close to those of **2**: $E_p^{\text{c, red}} = -2.28\text{ V}$ vs. (Fc⁺/Fc) (-2.29 V for **2**) and $E_{1/2}^{\text{ox}} = -0.02\text{ V}$ (0.02 V for **2**) at 0.2 V s^{-1} (Figure S5 in Supplementary Materials) indicating, as suggested previously by the IR analysis, that the replacement of the n-butyl group by the electron-withdrawing phenyl

does not modify significantly the redox behaviour of 1–2. The theoretical redox potential of the first electron transfer is -2.25 V for **1** and -2.28 V for **2**, in good agreement with the experimental values. The redox potential computed for the second electron transfer is -2.17 V and -2.16 V for **1** and **2**, respectively, indicating that this electron transfer is thermodynamically easier than the first, which also matches the electrochemical observations showing a two-electron reduction at slow scan rates (Figure S5c in Supplementary Materials).

2.2. DFT Investigations of the Geometries of the Mono-Anion and Di-Anion

In order to shed some light on the possible redox behaviour of the triazolylidene ligand in 1–2, the stereoelectronic features of the mono-anion and di-anion were investigated (Table S3 in Supplementary Materials).

The isomeric speciation of elusive mono-anion (**1⁻** and **2⁻**) and of di-anion (**1²⁻** and **2²⁻**) has been carried out to identify the structures of these ions that are likely present in solution. The flipping central methylene of propanedithiolate bridge is not predicted to significantly alter the thermodynamic speciation of reduced isomers (both **1⁻** and **2⁻**), so it has been neglected (however, we checked that the methylene flip has an associated $\Delta G = 0.8$ kcal/mol and 0.2 kcal/mol for the neutral **1** and **2**, respectively).

The relative stabilities of different geometries of **1⁻** (and **2⁻**) are reported in Figure 2A (Figure S6 in Supplementary Materials, for **2⁻**).

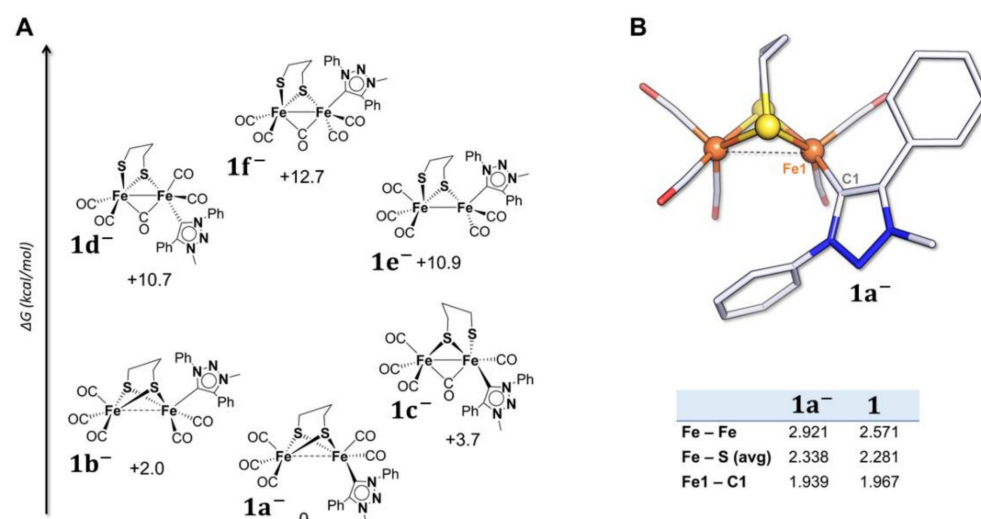


Figure 2. (A) Thermodynamic speciation of **1⁻** and (B) optimized structure of **1a⁻** with relevant geometrical parameters (distances in Å) in comparison with the ones of **1**. Atom coloring: Fe = orange, S = yellow, C = grey, N = blue, and O = red. H atoms are omitted for clarity. For simplification, net charges on structures are not reported.

The most stable computed structure of **1⁻** closely resembles that of **2⁻**, where the only structural variation observed is the elongation of the Fe–Fe bond. Other structural changes, such as Fe–S bond breaking or bridging of CO, are energetically prohibited or do not correspond to a minimum on the potential energy surface. Upon one-electron transfer of **1**, the triazolylidene preferentially adopts a basal position (the isomer **1a⁻** is 2 kcal/mol lower in energy than **1b⁻**, the isomer with the Pmpt ligand in the apical position). In the case of **2⁻**, there are no notable changes in the geometry of the complex and the Pmbt ligand keeps its basal position. The main difference between **1⁻** and **2⁻** is a slightly more elongated Fe–Fe distance in **1⁻**: a lengthening of 0.347 Å and 0.332 Å is observed in **1⁻** and **2⁻**, respectively. This is due to the antibonding character of the SOMO (Figure 3) of both mono-anions.

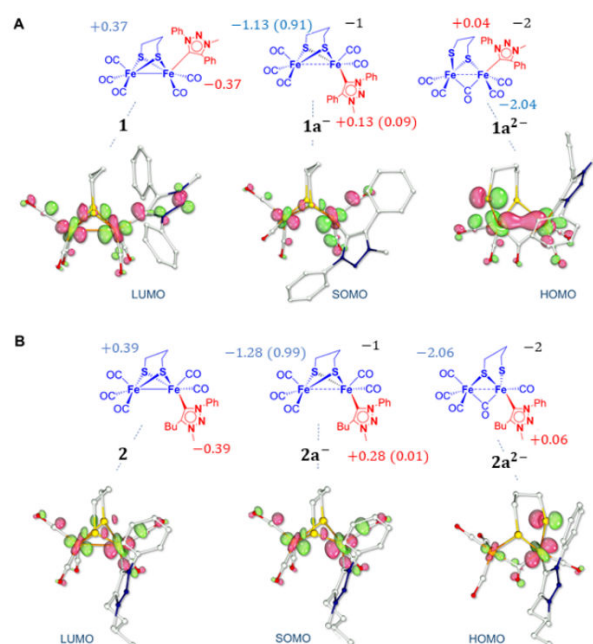


Figure 3. Natural Population Analysis (NPA) charges on the Pmpt (A) and Pmbt (B) ligands (red values) and on the rest of the complex for most stable neutral, anionic, and dianionic forms of **1** (A) and **2** (B). Spin densities (in electrons) calculated for **1a⁻** and **2a⁻** are reported in parenthesis. Bottom: Selected FMOs for the three redox states (isosurface cutoff: 0.05 a.u.).

The analysis of the SOMO of **1⁻** and **2⁻** shows that the molecular orbitals have a pure Fe_2S_2 character suggesting that the electron density is not located on the triazolylidene ligands upon one-electron transfer. Spin density calculation predicts that the unpaired electron is entirely delocalized on the bimetallic core, without participation of the Pmpt or Pmbt ligands, with a higher density on the iron atom bonded to the carbene and a strong orbital contribution of the two sulfur atoms. This is consistent with the LUMO shape and the electronic distribution in the neutral complexes, which is confined to the Fe-S region.

The DFT IR spectrum of **1⁻** (Table S1 in Supplementary Materials) also shows strict analogy with that of **2⁻**. The average value of the $\nu(\text{CO})$ is 1889 cm^{-1} (1870 cm^{-1} for **2⁻**) and agrees with the expected red-shift compared to the neutral complex. The extent of the shift, 76 cm^{-1} , is a bit less than that observed for **2⁻** (94 cm^{-1}), suggesting that the donor strength of the Pmpt ligand, in **1⁻**, is slightly weaker than that of Pmbt, in **2⁻**. Moreover, the extent of this shift is consistent with a strong enhancement of the electron density within the di-iron unit of the complexes which is confirmed by the spin density analysis (Figure 3). Indeed, the stereoelectronic features of both mono-anions suggest that MIC ligands do not play an active role in hosting electron density upon the first reduction since the extra electron density almost completely populates the di-iron core.

The different geometries considered for the structure of **1²⁻** are reported in Figure 4. Upon the second electron transfer, the breaking of one Fe-S bond is observed in the most stable isomer, **1a²⁻**. The resulting coordination vacancy is compensated by the migration of one basal CO to a bridging position between the two metal centres. This overall rearrangement is consistent with the electrochemical behaviour of **1**. The two distorted squared pyramidal geometries are held together by the bridging CO bond and one Fe-S bond, even if a weak iron-iron interaction is still present.

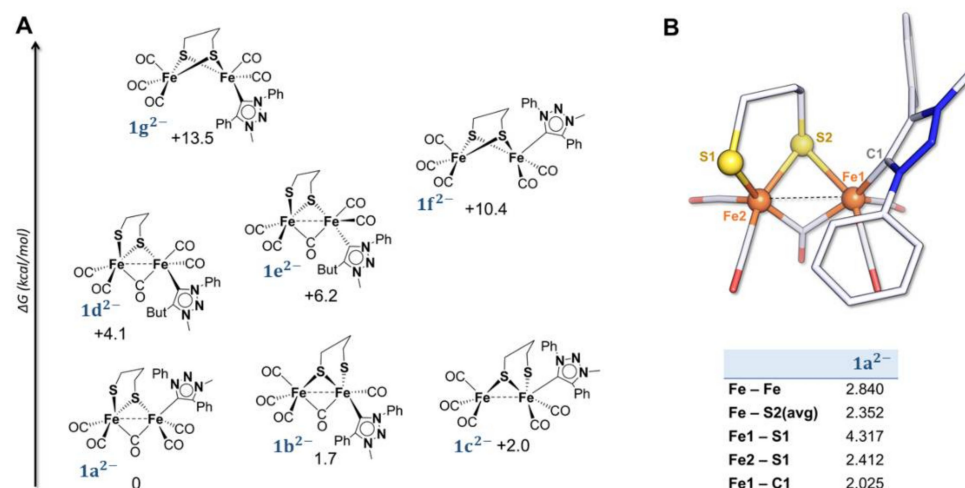


Figure 4. (A) thermodynamic speciation of 1^{2-} and (B) optimized structure of $1a^{2-}$ with relevant geometrical parameters (distances in Å). Atom coloring: Fe = orange, S = yellow, C = grey, N = blue, and O = red. H atoms are omitted for clarity. For simplification, net charges on structures are not reported.

The calculated structure of 1^{2-} (Figure 4) displays expected similarities to that of 2^{2-} (Figure S7 in Supplementary Materials). Nevertheless, it has to be noted that the cleaved Fe-S bond in 1^{2-} is different from that in 2^{2-} . Indeed, the breaking of one Fe-S bond can lead to different isomers since the two iron atoms are differently substituted. In the case of 1^{2-} , the most stable geometry presents a Fe-S bond cleavage with the $\{Fe(CO)_2(Pmpt)\}$ moiety, which is different from what is observed for 2^{2-} (Figure S7 in Supplementary Materials). Regardless of their different stereochemistry, the Fe-S cleavage in the two doubly reduced complexes is consistent with the ECE mechanism proposed on the CV basis. The theoretical IR spectrum of 1^{2-} (Table S1 in Supplementary Materials) is similar to that of 2^{2-} with a weak band at 1657 cm^{-1} (1646 cm^{-1} for 2^{2-}) that can be assigned to the asymmetrical stretching of the $\mu\text{-CO}$. A red-shift of 88 cm^{-1} (91 cm^{-1} for 2^{2-}) for the average value of $\nu(\text{CO})$ (1801 cm^{-1}) (1780 cm^{-1} for 2^{2-}) compared to that of 1^- (2^-) is expected. Such a strong shift suggests that the second electron transfer is centred at the Fe_2S_2 core. It is noteworthy that the HOMO of 1^{2-} (Figure 3A) is different from that calculated for 2^{2-} . It has mainly a Fe_2S_2 character with no contribution of the Pmpt ligand and it can be described as a combination of a σ_{FeFe} bonding orbital with a σ_{FeS}^* contribution. The HOMO of 2^{2-} , reported in Figure 3B, has also an almost pure Fe_2S_2 character with no involvement of the Pmpt ligand, but it corresponds to an overall σ_{2Fe2S}^* orbital with two different d_{Fe} orbitals and a σ_{Fe-S}^* contribution. The charge distribution within the complex is -2.04 for 1^{2-} (-2.06 for 2^{2-}) on the iron core and $+0.04$ on the Pmpt ligand ($+0.06$ on Pmbt). Comparing the negative charge distribution of the di-anion to that computed for the mono-anion and neutral form, one can conclude that the di-iron core hosts most of the electron density upon the first and second electron transfers. The triplet spin state ($S = 1$), with an unpaired electron at the Fe-S region and one distributed over Pmpt, is 14 kcal/mol (13.6 kcal/mol for Pmbt) less stable than the singlet spin state ($S = 0$), further stressing the low tendency of Pmpt (Pmbt) to accommodate electron density upon reduction.

2.3. In Silico Modification of the MIC Ligand

The Pmpt carbene, even with two electron-withdrawing phenyl groups, turns out to not be likely to host additional electron density from reduction. Indeed, the electron transfers are exclusively Fe_2S_2 centred for both the neutral and anionic forms due to the absence of hybrid metal ligand molecular orbital establishing electronic communication. Further modifications of the MIC ligand have been considered in a silico DFT approach to predict how the relevant stereoelectronic features of such di-iron species could be modulated. The

DFT structure of 1^- has been modified by systematically adding an increasing number of powerful electron-withdrawing element/group such as fluorine atoms in different positions on the aromatic rings of the Pmpt ligand (Figure 5, top). The spin density values have been calculated (Figure 5, bottom) to determine the distribution of the unpaired electron density over the entire molecular structure.

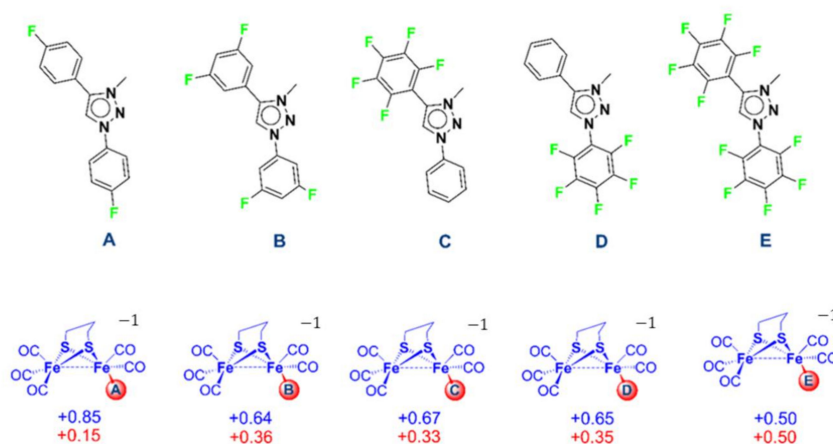


Figure 5. Structure of the Pmpt ligand variants tested (A–E, top), with the corresponding spin density values (in electrons, bottom) calculated for the anionic form of the corresponding mono-substituted complexes (spin density on the modified Pmpt ligands is reported in red, while the one on the rest of the complex comprising the Fe₂S₂ core is in blue).

The data show that the systematic replacement of hydrogen by fluorine atoms in the phenyl rings of the triazolylidene should trigger and then proportionally increase the delocalization of the electron density in the reduced (anionic) form. A significant electron delocalization is only obtained with, at least, four fluorine atoms (B, C, and D forms). Moreover, it has to be emphasized that even with a fully perfluorinated Pmpt ligand, the electron transfer is not exclusively located on the triazolylidene, suggesting that a genuine non-innocence of such carbene ligands is questionable and still an open question.

2.4. DFT Investigations of Protonation and Electron Steps in the Proposed Electrocatalytic Pathway

Despite the fact that the electrocatalytic activities of **2** towards proton reduction are inefficient or non-existent, DFT calculations were performed, using **2** as a model of di-iron site linked to a MIC ligand, to find out which electron and proton transfers are energetically preferred in the processes involving such species. Indeed, since di-iron complexes featuring MIC or NHC ligands have comparable activity and redox behaviour, they may similarly be involved in the electrocatalytic HER process [30,33,47,48]. This approach may highlight the reactivity flaws of such species and inspire the design of more efficient complexes with MIC or NHC ligands. The study of the catalytic cycle for the proton reduction was carried out (DFT methodological details are provided in Materials and Methods).

First, three geometries have been considered for the species $2H^-$ arising from the protonation of 2^{2-} (Figure 6A).

The breaking of one Fe–S bond leads to a possible S-protonation in reason of the available lone pair (Figure 6A,B, $2Hb^-$). The barriers of activation for the processes leading to the three geometries have been calculated and it turns out that the direct formation of hydride species ($2Ha^-$ —in which the hydride is coordinated to the two metal centres in a bridging mode and $2Hc^-$ —in which the hydride is terminally coordinated to a single iron atom) by protonation of the di-iron site is kinetically rather impeded. The mutual comparison of energy barriers (Figure 6A) suggests that the first step of the mechanism is probably the S-protonation (lowest activation barrier), followed by an intramolecular proton transfer to the di-iron site, generating the bridging hydride species, thermodynamically more stable. The value of the energy barrier for this proton migration $\{Fe_2SH\} \rightarrow \{Fe_2(\mu-H)\}$

($2\text{Hb}^- \rightarrow 2\text{Ha}^-$) is +14.2 kcal/mol. It may involve the formation of the transient terminal hydride species 2Hc^- that finally isomerizes into the bridging hydride form 2Ha^- . The computed structure of the thermodynamic product 2Ha^- is mainly characterized by the presence of a bridging hydride in a quasi-symmetrical coordination between the two iron atoms (Fe1–H = 1.694 Å, and Fe2–H = 1.665 Å). The geometry around both iron atoms is octahedral, with an evident distortion of the dithiolate bridge. In the S-protonated species 2Hb^- , the S–H bond distance is 1.367 Å while it is 1.495 Å in the transition state. The ΔG estimated for the protonation is -10.8 kcal/mol with a ΔG^\ddagger of +5.2 kcal/mol, consistently with a facile and fast reaction.

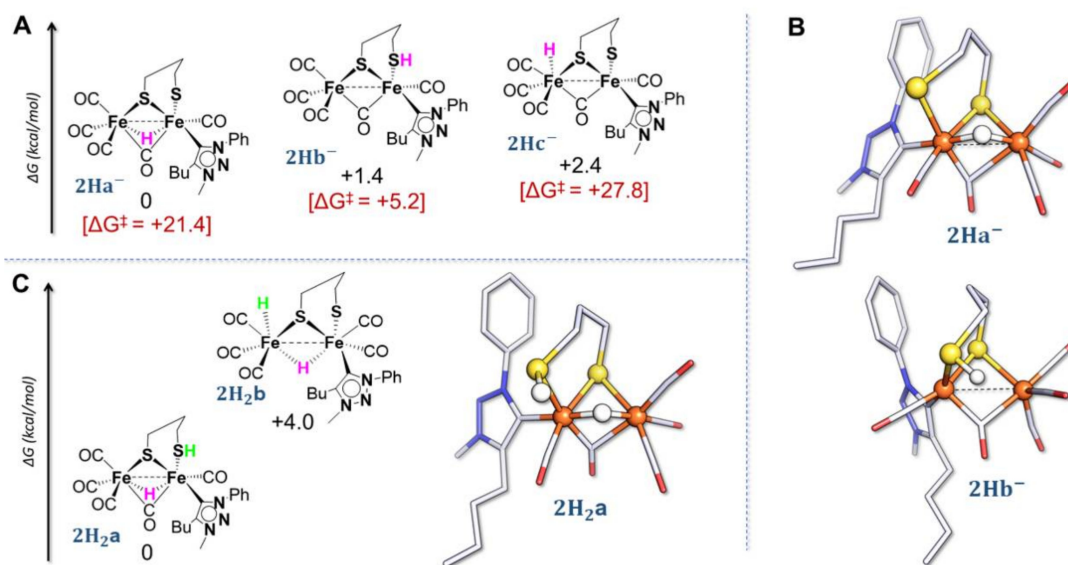


Figure 6. (A) thermodynamic speciation of 2H^- . Furthermore, the activation barrier associated with the formation of each protonated form are reported (red values). (B) optimized structure of thermodynamic (2Ha^-) and kinetic (2Hb^-) products of the first protonation. (C) thermodynamic speciation of 2H_2 and optimized structure of $2\text{H}_2\text{a}$. Atom coloring: Fe = orange, S = yellow, C = grey, N = blue, and O = red. H atoms are omitted for clarity. For simplification, net charges on structures are not reported.

Two possible structures have been found for the species arising from the second protonation (Figure 6C). The DFT structure of the thermodynamically stable neutral di-protonated species $2\text{H}_2\text{a}$ resembles the previous structure proposed for 2Ha^- but with a protonated S atom. The structure of the second isomer, $2\text{H}_2\text{b}$, is characterized by the presence of a bridging hydride and a terminal hydride at the $\{\text{Fe}(\text{CO})_3\}$ moiety and the absence of a bridging CO. $2\text{H}_2\text{a}$ is notably more stable than the dihydride form. The S–H length is 1.353 Å and the distance between the two H atoms is 2.773 Å. If the species $2\text{H}_2\text{a}$ is considered in the proton reduction process, the final formation of H_2 would involve a proton–hydride coupling $\{\text{S}-\text{H} \cdots \text{H}-\text{Fe}\}$. However, the $\text{H} \cdots \text{H}$ distance and the unfavorable spatial orientation require a strong distortion in the metal coordination sphere for the formation and the release of H_2 . The value of the energy barrier is indeed $+18.1$ kcal mol $^{-1}$ which is rather high (the computed rate constant is 4.0 s $^{-1}$). This result agrees with the essentially low (or even absent) catalytic activity of such a complex.

Figure 7 resumes the putative DFT mechanism of proton reduction mediated by **2**.

The two electron transfers centred on the di-iron core trigger the cleavage of a Fe–S bond with the concomitant bridging of a CO between iron atoms. DFT calculations suggest that the first protonation of the mechanism is a S-protonation, leading to the isomer 2Hb^- that, subsequently, isomerizes to the thermodynamically more stable isomer 2Ha^- with a bridging hydride.

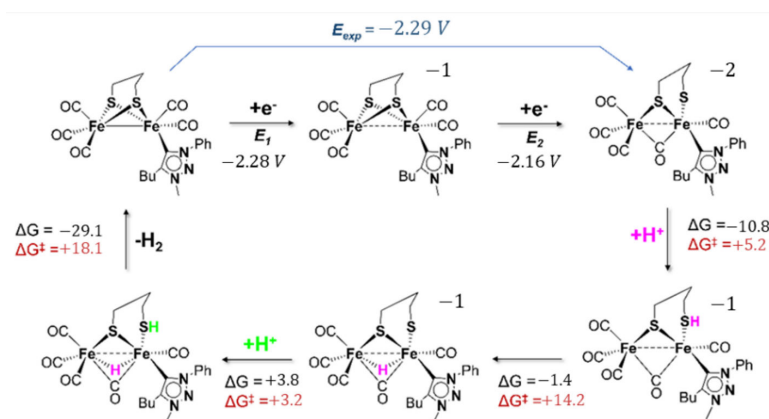


Figure 7. Proposed catalytic cycle for proton reduction.

A further S-protonation affords **2H₂a** that is able through a proton–hydride interaction {S-H ··· H-Fe} to release H₂. This last step is predicted to be the rate-determining step due to the relatively high value of the energy barrier (vide supra). Due to the lack of electronic communication between the ligand and the di-iron core in **2⁻** and **2²⁻** and the absence of any obvious involvement during the catalytic cycle, it can be proposed that the ligand Pmbt, in **2**, has a redox innocent behaviour.

Finally, the poor catalytic activity (if any) towards proton reduction of the Pmbt derivative may be associated with a slow formation and release of H₂, probably due to a regiochemically impeded H⁺-H⁻ hetero-coupling during the last step of the catalytic cycle.

3. Materials and Methods

All the experiments were carried out under an inert atmosphere, using Schlenk techniques for the syntheses. Solvents were deoxygenated and dried according to standard procedures. The iron precursor [Fe₂(CO)₆(μ-pdt)] [49] and Pmpt = 1-phenyl-3-methyl-4-phenyl-1,2,3-triazol-5-ylidene [42] were prepared according to literature procedures. All other reagents were commercially available and used as purchased. NMR spectra (¹H and ¹³C) were recorded with Bruker DRX500 spectrometer of the “Service général des plateformes, Université de Bretagne Occidentale, Brest” and were referenced to SiMe₄ (¹H) and H₃PO₄ (³¹P). The infrared spectra were recorded on a FT IR VERTEX 70 Bruker spectrometer. Chemical analyses were made by the “Service de Microanalyse I.C.S.N.”, Gif sur Yvette (France). Electrochemical measurements were conducted using a PG-STAT 128 N Autolab or a μ-autolab (type III) electrochemical analyzer driven by the GPES software. All the electrochemical studies were carried out in a conventional three-electrode cell under an inert atmosphere (argon). The preparation and the purification of the supporting electrolyte [Bu₄N][PF₆] were as described previously [50]. The working electrode was a vitreous carbon disk of 0.3 cm in diameter, polished with alumina prior to use. A platinum wire was used as counter electrode. The reference electrode was an Ag|Ag⁺ electrode, however, all the potentials (text, tables, and figures) are quoted against the (Fc⁺/Fc) couple; ferrocene was added as an internal standard at the end of the experiments. Crystal data for compound **1** were collected on an Oxford Diffraction X-Calibur-2 CCD diffractometer, equipped with a jet cooler device and graphite-monochromated Mo-Kα radiation (λ = 0.71073 Å). The structure was solved and refined by standard procedures [51]. Deposition number CCDC 2179366 contain the supplementary crystallographic data for **1**. These data can also be obtained free of charge from the Cambridge Crystallographic Data Centre via www.ccdc.cam.ac.uk/data_request/cif (accessed on 15 June 2022).

Calculations have been performed using the TURBOMOLE 7.4.1 suite of programs [52]. A triple-ζ TZVP basis (for all atoms) and the pure functional BP86 were used [53–55]. This particular basis-set/functional combination has been widely validated in the context of Fe/Ni-thiolate bioinorganic and biomimetic systems, also in relation to hydrogenases [56–59]. The Resolution-of-Identity (RI) technique allowed us to speed up geometry optimizations [60].

Grimme's corrections with Becke–Johnson damping (D3BJ) were added to account for dispersive interactions [61,62]. COSMO was used to implicitly treat the solvent, by setting a $\epsilon_r = 8.93$ of CH_2Cl_2 [63,64]. The nature of each stationary point was verified by means of full vibrational analysis. Atomic charges and spin densities were calculated performing a Natural Population Analysis (NPA) as implemented in the Natural Bond Orbital (NBO) procedure. The total partition function (Q) has been evaluated as a product of q-rotational, q-translational, and q-vibrational contributions and used to derive free energies from SCF energy values, by setting temperature and pressure to 298.15 K and 1 bar, respectively (the scaling factor for the SCF wavenumbers has been set to 0.9914, as default value in TURBOMOLE for the adopted theoretical scheme). In-solvent free energies were used to calculate absolute redox potentials of the couple under investigation, according to the relation $E^\circ = -\Delta G^\circ / nF$ (n = number of electrons involved in the redox process; F = Faraday constant), which were then scaled by a reference value (-5.08 V for the Fc^+/Fc couple, calculated at the same level of theory).

4. Conclusions

The two complexes $[\text{Fe}_2(\text{CO})_5(\text{MIC})(\mu\text{-pdt})]$ (**1,2**) have been prepared and studied in order to describe the effect of mesoionic carbenes on the behaviour of such di-iron systems. The two triazolylidenes, which were used, differ by a phenyl group (in **1**) instead of a butyl group (in **2**). This change affects the relative stability of basal, apical isomers related to the position of the carbene. The different DFT-predicted stable isomers, with apical and basal position of this ligand, are observed in solid state for **1** and **2**, respectively. Spectroscopic and electrochemical characterization show the close and good σ -donation ability of these triazole-based carbenes, by increasing the electron density of the di-iron site. DFT investigations addressed the question of the redox, innocent or non-innocent, properties of these ligands by examining the electronic structure of mono- and di-anion of **1,2**. They show that MIC ligands lying in the first coordination sphere of a carbonyl di-iron dithiolate core feature innocent redox behaviour. The replacement of the butyl by a phenyl group in the triazole cycle is insufficient to trigger the electronic communication between the triazolylidene and the di-iron core. Moreover, only significant perfluorination of the phenyl groups carried by the triazole cycle allows the partial distribution of the electronic density over various atomic centres. This observation may afford interesting perspectives for the design of new triazole systems endowed with a non-innocent redox behaviour.

Finally, the importance of the sulfur environment is highlighted by DFT when considering the protonation processes after the transfer of two electrons. On the one hand, S-protonation facilitates the formation of required hydride species for HER evolution, affording a proton relay but, on the other hand, intermediates featuring $\{\text{Fe} \cdots \text{H} \cdots \text{H} \cdots \text{S}\}$ do not favor the release of H_2 , suggesting the reason why **1,2** are not efficient for HER catalysis.

Supplementary Materials: The following supporting information can be downloaded at: <https://www.mdpi.com/article/10.3390/molecules27154700/s1>, Figure S1: Geometry of complexes **1, 2**; Figure S2: IR spectrum of **1** in CH_2Cl_2 ($\nu(\text{CO})$ region); Figure S3: ^1H NMR spectrum of **1** in CD_2Cl_2 ; Figure S4: $^{13}\text{C}\{^1\text{H}\}$ NMR spectrum of **1** in CD_2Cl_2 ; Figure S5: (a) Cyclic voltammograms of **1** (1.9 mM), CH_2Cl_2 - $[\text{NBu}_4][\text{PF}_6]$ (0.2 M) under Ar at 0.2 V s^{-1} . (b) Variation of the current intensity (I_p) as a function of the square root of the scan rate ($\nu^{1/2}$). (c) Scan rate dependence of the current for the reduction of **1** in CH_2Cl_2 - $[\text{NBu}_4][\text{PF}_6]$ (0.2 M) (vitreous carbon electrode); Figure S6: (A) thermodynamic speciation of 2^- and (B) optimized structure of $2a^-$ with relevant geometrical parameters (distances in Å) in comparison with the ones of its neutral counterpart **2**. Atom coloring: Fe = orange, S = yellow, C = grey, N = blue, and O = red. H atoms are omitted for clarity. For simplification, net charges on structures are not reported.; Figure S7: (A) thermodynamic speciation of 2^{2-} and (B) optimized structure of $2a^{2-}$ with relevant geometrical parameters (distances in Å). Atoms coloring: Fe = orange, S = yellow, C = grey, N = blue, and O = red. H atoms are omitted for clarity. For simplification, net charges on structures are not reported; Table S1: Calculated $\nu(\text{CO})$ (cm^{-1}) of complexes **1** and **2** and their most stable mono-anion and di-anion of **1** and **2**; Table S2:

Crystallographic data and refinement parameters of **1**.C₄H₈O; Table S3: XYZ Coordinates of selected optimized structures.

Author Contributions: Synthetic work, X-ray and spectroscopic characterizations, and electrochemical study were carried out by A.M. with input from C.E. and P.S. DFT calculations were performed by A.M. with input from F.A. and G.Z. The manuscript was written jointly by F.A., G.Z., C.E., F.Y.P., and P.S. All authors have read and agreed to the published version of the manuscript.

Funding: This research was funded by the European Union Marie Skłodowska-Curie Initial Training Network NoNoMeCat project (675020-H2020-MSCA-ITN-2015).

Institutional Review Board Statement: Not applicable.

Informed Consent Statement: Not applicable.

Data Availability Statement: The data presented in this study are available in supplementary material.

Acknowledgments: CNRS (Centre National de la Recherche Scientifique), the Université de Bretagne Occidentale, are acknowledged for financial support. We are grateful to F. Michaud for the crystallographic measurements of **1** and to the ‘Service général des plateformes, Brest’ for NMR measurements on the Bruker DRX 500 spectrometer. We thank M. Albrecht and S. Bertini for their help for the preparation of MIC ligands.

Conflicts of Interest: The authors declare no conflict of interest.

Sample Availability: Samples of the compounds are not available from the authors.

Appendix A

Synthesis of [Fe₂(CO)₅(Pmpt)(μ-pdt)] (1)

A solution of [Fe₂(CO)₆(μ-pdt)] (200 mg, 0.518 mmol) with an excess of 1-phenyl-3-methyl-4-phenyl-1,2,3-triazol-5-ylidene, Pmpt, (300 mg, 1.28 mmol) was prepared in degassed anhydrous THF (25 mL). 144 mg of potassium tert-butoxide (1.28 mmol) were added at 0 °C under vigorous stirring and the mixture was stirred for 30 min. The solvent was evaporated under reduced pressure to dryness and then 10 mL of CH₂Cl₂ were added. The resulting red solution was filtered over Celite and evaporated to dryness to yield **1** as a red powder (184 mg, 60%). Crystallization by slow diffusion at −35 °C (hexane/THF 1:1) afforded red single crystals suitable for X-ray diffraction analysis.

IR (CH₂Cl₂, cm^{−1}): ν(CO) 2033(s), 1968(vs), 1945(sh), 1910(w)

¹H NMR (CD₂Cl₂, δ, ppm): δ 7.70; 7.60; 7.57 (m, 10H, N-Ph and Ph), 3.90 (s, 3H, CH₃), 1.78 (2H, m, pdt), 1.63 (4H, m, pdt)

¹³C-¹H NMR (CD₂Cl₂, δ, ppm): 216.4 (s, CO), 212.1 (s, CO), 173.3 (s, Fe-CMIC), {149.6, 140.9, 131.8, 130.4, 129.1, 128.4} (C₆H₅ + N-C₆H₅), 37.60, 29.9, 24.3 (NCH₃ + S(CH₂)₃S)

Elemental Analysis calculated for C₂₃H₁₉Fe₂N₃O₅S₂: 46.54% C, 3.20% H, 7.08% N. Found: 46.11% C, 3.33% H, 6.98% N.

References

1. Peters, J.W.; Lanzilotta, W.N.; Lemon, B.J.; Seefeldt, L.C. X-ray Crystal Structure of the Fe-Only Hydrogenase (Cpl) from *Clostridium pasteurianum* to 1.8 Å Resolution. *Science* **1998**, *282*, 1853–1858. [[CrossRef](#)] [[PubMed](#)]
2. Nicolet, Y.; Piras, C.; Legrand, P.; Hatchikian, C.E.; Fontecilla-Camps, J.C. Desulfovibrio desulfuricans iron hydrogenase: The structure shows unusual coordination to an active site Fe binuclear center. *Structure* **1999**, *7*, 13–23. [[CrossRef](#)]
3. Berggren, G.; Adamska, A.; Lambert, C.; Simmons, T.R.; Esselborn, J.; Atta, M.; Gambarelli, S.; Mouesca, J.M.; Reijerse, E.; Lubitz, W.; et al. Biomimetic assembly and activation of [FeFe]-hydrogenases. *Nature* **2013**, *4*, 66–70. [[CrossRef](#)] [[PubMed](#)]
4. Lubitz, W.; Ogata, H.; Rüdiger, O.; Reijerse, E. Hydrogenases. *Chem. Rev.* **2014**, *114*, 4081–4148. [[CrossRef](#)]
5. Wittkamp, F.; Senger, M.; Stripp, S.T.; Apfel, U.-P. [FeFe]-Hydrogenases: Recent developments and future perspectives. *Chem. Commun.* **2018**, *54*, 5934–5942. [[CrossRef](#)]
6. Laun, K.; Baranova, I.; Duan, J.; Kertess, L.; Wittkamp, F.; Apfel, U.-P.; Happe, T.; Senger, M.; Stripp, S.T. Site-selective protonation of the one-electron reduced cofactor in [FeFe]-hydrogenase. *Dalton Trans.* **2021**, *50*, 3641–3650. [[CrossRef](#)]
7. Birrell, J.A.; Rodríguez-Maciá, P.; Reijerse, E.J.; Martini, M.A.; Lubitz, W. The catalytic cycle of [FeFe] hydrogenase: A tale of two sites. *Coord. Chem. Rev.* **2021**, *449*, 214191–214213. [[CrossRef](#)]

8. Caserta, G.; Zuccarello, L.; Barbosa, C.; Silveira, C.M.; Moe, E.; Katz, S.; Hildebrandt, P.; Zebger, I.; Todorovic, S. Unusual structures and unknown roles of FeS clusters in metalloenzymes seen from a resonance Raman spectroscopic perspective. *Coord. Chem. Rev.* **2022**, *452*, 214287–214299. [[CrossRef](#)]
9. Apfel, U.-P.; Pétilion, F.Y.; Schollhammer, P.; Talarmin, J.; Weigand, W. [FeFe] hydrogenase models: An overview. In *Bioinspired Catalysis: Metal-Sulfur Complexes*; Weigand, W., Schollhammer, P., Eds.; Wiley-VCH-Verl: Weinheim, Germany, 2015; pp. 79–103, ISBN 978-3-527-33308-0.
10. Elleouet, C.; Pétilion, F.Y.; Schollhammer, P. [FeFe]-hydrogenases models. In *Advances in Bioorganometallic Chemistry: [FeFe]-Hydrogenases Models*; Hirao, T., Moriuchi, T., Eds.; Elsevier: Amsterdam, The Netherlands, 2019; Chapter 17; pp. 347–359, ISBN 9780128141984.
11. Schilter, D.; Camara, J.M.; Huynh, M.T.; Hammes-Schiffer, S.; Rauchfuss, T.B. Hydrogenase enzymes and their synthetic models: The role of metal hydrides. *Chem. Rev.* **2016**, *116*, 8693–8749. [[CrossRef](#)]
12. Simmons, T.R.; Berggren, G.; Bacchi, M.; Fontecave, M.; Artero, V. Mimicking hydrogenases: From biomimetics to artificial enzymes. *Coord. Chem. Rev.* **2014**, *270–271*, 127–150. [[CrossRef](#)]
13. Zhang, X.; Liu, L.; Cao, W.; Lv, D. Di-iron analogue of [FeFe]-hydrogenase active site as a molecular electro-catalyst for proton reduction. *Catal. Lett.* **2020**, *150*, 3409–3414. [[CrossRef](#)]
14. Van Beek, C.B.; van Leest, N.P.; Lutz, M.; de Vos, S.D.; Klein Gebbink, R.J.M.; de Bruin, B.; Broere, D.L.J. Combining metal–metal cooperativity, metal–ligand cooperativity and chemical non-innocence in diiron carbonyl complexes. *Chem. Sci.* **2022**, *13*, 2094–2104. [[CrossRef](#)]
15. Capon, J.-F.; Gloaguen, F.; Pétilion, F.Y.; Schollhammer, P.; Talarmin, J. Organometallic diiron complex chemistry related to the [2Fe]H subsite of [FeFe]H₂ase. *Eur. J. Inorg. Chem.* **2008**, *2008*, 4671–4681. [[CrossRef](#)]
16. Chouffai, D.; Zampella, G.; Capon, J.-F.; De Gioia, L.; Le Goff, A.; Pétilion, F.Y.; Schollhammer, P.; Talarmin, J. Electrochemical and theoretical studies of the impact of the chelating ligand on the reactivity of [Fe₂(CO)₄(κ²-LL)(μ-pdt)]⁺ complexes with different substrates (LL = I_{Me}-CH₂-I_{Me}, dppe; I_{Me} = 1-Methylimidazol-2-ylidene). *Organometallics* **2012**, *31*, 1082–1091. [[CrossRef](#)]
17. Chouffai, D.; Capon, J.-F.; De Gioia, L.; Pétilion, F.Y.; Schollhammer, P.; Talarmin, J.; Zampella, G. A diferrous dithiolate as a model of the elusive Hox^{inact} state of the [FeFe] hydrogenases: An electrochemical and theoretical dissection of its redox chemistry. *Inorg. Chem.* **2015**, *54*, 299–311. [[CrossRef](#)]
18. Morvan, D.; Capon, J.-F.; Gloaguen, F.; Le Goff, A.; Marchivie, M.; Michaud, F.; Schollhammer, P.; Talarmin, J.; Yaouanc, J.-J.; Pichon, R.; et al. N-heterocyclic carbene ligands in nonsymmetric diiron models of hydrogenase active sites. *Organometallics* **2007**, *26*, 2042–2052. [[CrossRef](#)]
19. Orain, P.-Y.; Capon, J.-F.; Gloaguen, F.; Pétilion, F.Y.; Schollhammer, P.; Talarmin, J.; Zampella, G.; De Gioia, L.; Roisnel, T. Investigation on the protonation of a trisubstituted [Fe₂(CO)₃(PPh₃)(κ²-phen)(μ-pdt)] complex: Rotated versus unrotated intermediate pathways. *Inorg. Chem.* **2010**, *49*, 5003–5008. [[CrossRef](#)]
20. Orain, P.-Y.; Capon, J.-F.; Kervarec, N.; Gloaguen, F.; Pétilion, F.Y.; Pichon, R.; Schollhammer, P.; Talarmin, J. Use of 1,10-phenanthroline in diiron dithiolate derivatives related to the [Fe–Fe] hydrogenase active site. *Dalton Trans.* **2007**, 3754–3756. [[CrossRef](#)]
21. Arrigoni, F.; Elleouet, C.; Mele, A.; Pétilion, F.Y.; De Gioia, L.; Schollhammer, P.; Zampella, G. Insights into the two-electron reductive process of [FeFe]H₂ase biomimetics: Cyclic voltammetry and DFT investigation on chelate control of redox properties of [Fe₂(CO)₄(κ²-chelate)-(μ-dithiolate)]. *Chem. Eur. J.* **2020**, *26*, 17536–17545. [[CrossRef](#)]
22. Hu, S.-P.; Zhang, L.; Wu, Y.; Feng, J.-S.; Wu, S.; Xie, B.; Zou, L.-K. [FeFe]-hydrogenase active site mimics containing pyridyl-functionalized phosphine ligands: Synthesis, characterization and electrochemical investigation. *Inorg. Chim. Acta* **2020**, *504*, 119435–119441. [[CrossRef](#)]
23. Schippers, E.C.F.; Nurttila, S.S.; Oudsen, J.-P.H.; Tromp, M.; Dzik, W.I.; van der Vlugt, J.I.; Reek, J.N.H. [FeFe]-hydrogenase mimic employing κ²-C, N-pyridine bridgehead catalyzes proton reduction at mild overpotential. *Eur. J. Inorg. Chem.* **2019**, *2019*, 2510–2517. [[CrossRef](#)]
24. Roy, S.; Groy, T.L.; Jones, A.K. Biomimetic model for [FeFe]-hydrogenase: Asymmetrically disubstituted diiron complex with a redox-active 2,2'-bipyridyl ligand. *Dalton Trans.* **2013**, *42*, 3843–3853. [[CrossRef](#)]
25. Merinero, A.D.; Collado, A.; Casarrubios, L.; Gómez-Gallego, M.; Ramírez de Arellano, C.; Caballero, A.; Zapata, F.; Sierra, M.A. Triazole-containing [FeFe] hydrogenase mimics: Synthesis and electrocatalytic behaviour. *Inorg. Chem.* **2019**, *58*, 16267–16278. [[CrossRef](#)]
26. Pandey, I.K.; Agarwal, T.; Mobin, S.M.; Stein, M.; Kaur-Ghumaan, S. Switching site reactivity in hydrogenase model systems by introducing a pendant amine ligand. *ACS Omega* **2021**, *6*, 4192–4203. [[CrossRef](#)]
27. Becker, R.; Amirjalayer, S.; Li, P.; Woutersen, S.; Reek, J.N.H. An iron-iron hydrogenase mimic with appended electron reservoir for efficient proton reduction in aqueous media. *Sci. Adv.* **2016**, *2*, e1501014. [[CrossRef](#)]
28. Camara, J.M.; Rauchfuss, T.B. Combining acid–base, redox and substrate binding functionalities to give a complete model for the [FeFe]-hydrogenase. *Nat. Chem.* **2012**, *4*, 26–30. [[CrossRef](#)]
29. Liu, Y.-C.; Yen, T.-H.; Tseng, Y.-J.; Hu, C.-H.; Lee, G.H.; Chiang, M.-H. Electron delocalization from the fullerene attachment to the diiron core within the active-site mimics of [FeFe]hydrogenase. *Inorg. Chem.* **2012**, *51*, 5997–5999. [[CrossRef](#)]

30. Tye, J.W.; Lee, J.; Wang, H.-W.; Mejia-Rodriguez, R.; Reibenspies, J.H.; Hall, M.B.; Darensbourg, M.Y. Dual electron uptake by simultaneous iron and ligand reduction in an N-Heterocyclic Carbene substituted [FeFe] hydrogenase model compound. *Inorg. Chem.* **2005**, *44*, 5550–5552. [[CrossRef](#)]
31. Song, L.C.; Luo, X.; Wang, Y.-Z.; Gai, B.; Hu, Q.-M. Synthesis, characterization and electrochemical behavior of some N-heterocyclic carbene-containing active site models of [FeFe]-hydrogenases. *J. Organomet. Chem.* **2009**, *694*, 103–112. [[CrossRef](#)]
32. Schwab, D.E.; Tard, C.; Brecht, E.; Peters, J.W.; Pickett, C.J.; Szilagyi, R.K. On the electronic structure of the hydrogenase H-cluster. *Chem. Commun.* **2006**, 3696–3698. [[CrossRef](#)]
33. Capon, J.-F.; El Hassnaoui, S.; Gloaguen, F.; Schollhammer, P.; Talarmin, J. N-Heterocyclic Carbene Ligands as Cyanide Mimics in Diiron Models of the All-Iron Hydrogenase Active Site. *Organometallics* **2005**, *24*, 2020–2022. [[CrossRef](#)]
34. Orton, G.R.F.; Ghosh, S.; Alker, L.; Sarker, J.C.; Pugh, D.; Richmond, M.G.; Hartl, F.; Hogarth, G. Biomimics of [FeFe]-hydrogenases incorporating redox-active ligands: Synthesis, redox properties and spectroelectrochemistry of diiron-dithiolate complexes with ferrocenyl-diphosphines as Fe₄S₄ surrogates. *Dalton Trans.* **2022**, *51*, 9748–9769. [[CrossRef](#)] [[PubMed](#)]
35. Ghosh, S.; Rana, S.; Hollingsworth, N.; Richmond, M.G.; Kabir, S.E.; Hogarth, G. Hydrogenase Biomimetics with Redox-Active Ligands: Synthesis, Structure, and Electrocatalytic Studies on [Fe₂(CO)₄(κ²-dppn)(μ-edt)] (edt = Ethanedithiolate; dppn = 1,8-bis(Diphenylphosphino)Naphthalene). *Inorganics* **2018**, *6*, 122. [[CrossRef](#)]
36. Vivancos, A.; Segarra, C.; Albrecht, M. Mesoionic and related less heteroatom-stabilized N-Heterocyclic Carbene complexes: Synthesis, catalysis, and other applications. *Chem. Rev.* **2018**, *118*, 9493–9586. [[CrossRef](#)]
37. Guisado-Barrios, G.; Soleilhavoup, M.; Bertrand, G. 1H-1,2,3-Triazol-5-ylidenes: Readily available mesoionic carbenes. *Acc. Chem. Res.* **2018**, *51*, 3236–3244. [[CrossRef](#)]
38. Guisado-Barrios, G.; Bouffard, J.; Donnadiou, B.; Bertrand, G. Crystalline 1H-1,2,3-triazol-5-ylidenes: New stable mesoionic carbenes (MICs). *Angew. Chem. Int. Ed.* **2019**, *49*, 4759–4762. [[CrossRef](#)]
39. Albrecht, M. C4-bound imidazolylidenes: From curiosities to high-impact carbene ligands. *Chem. Commun.* **2008**, 3601–3610. [[CrossRef](#)]
40. Mathew, P.; Neels, A.; Albrecht, M. 1,2,3-Triazolylidenes as versatile abnormal carbene ligands for late transition metals. *J. Am. Chem. Soc.* **2008**, *130*, 13534–13535. [[CrossRef](#)]
41. Albrecht, M. Carbene in action. *Science* **2009**, *326*, 532–533. [[CrossRef](#)]
42. Sanghi, S.; Willett, E.; Versek, C.; Tuominen, M.; Coughlin, E.B. Physicochemical properties of 1,2,3-triazolium ionic liquids. *RSC Adv.* **2012**, *2*, 848–853. [[CrossRef](#)]
43. Mele, A.; Bertini, S.; Albrecht, M.; Elleouet, C.; Pétilion, F.Y.; Schollhammer, P. A diiron hydrogenase mimic featuring a 1,2,3-triazolylidene. *Chimia* **2020**, *74*, 499–503. [[CrossRef](#)]
44. Maity, R.; Sarkar, B. Chemistry of compounds based on 1,2,3-triazolylidene-type mesoionic carbenes. *JACS Au* **2022**, *2*, 22–57. [[CrossRef](#)]
45. Huynh, H.V. Electronic properties of N-Heterocyclic Carbenes and their experimental determination. *Chem. Rev.* **2018**, *118*, 9457–9492. [[CrossRef](#)]
46. Poulain, A.; Canseco-Gonzalez, D.; Hynes-Roche, R.; Muller-Bunz, H.; Schuster, O.; Stoeckli-Evans, H.; Neels, A.; Albrecht, M. Synthesis and tunability of abnormal 1,2,3-triazolylidene palladium and rhodium complexes. *Organometallics* **2011**, *30*, 1021–1029. [[CrossRef](#)]
47. Riener, K.; Haslinger, S.; Raba, A.; Högerl, M.P.; Cokoja, M.; Herrmann, W.A.; Kühn, F.E. Chemistry of iron N-Heterocyclic Carbene complexes: Syntheses, structures, reactivities, and catalytic applications. *Chem. Rev.* **2014**, *114*, 5215–5272. [[CrossRef](#)]
48. Jiang, S.; Liu, J.; Shi, Y.; Wang, Z.; Åkermark, B.; Sun, L. Preparation, characteristics and crystal structures of novel N-heterocyclic carbene substituted furan- and pyridine-containing azadithiolate Fe–S complexes. *Polyhedron* **2007**, *26*, 1499–1504. [[CrossRef](#)]
49. Lyon, E.J.; Georgakaki, I.P.; Reibenspies, J.H.; Darensbourg, M.Y. Carbon monoxide and cyanide Ligands in a classical organometallic complex model for Fe-only hydrogenase. *Angew. Chem. Int. Ed.* **1999**, *38*, 3178–3180. [[CrossRef](#)]
50. Arrigoni, F.; Mohamed Bouh, S.; Elleouet, C.; Pétilion, F.Y.; Schollhammer, P.; De Gioia, L.; Zampella, G. Electrochemical and theoretical investigations of the oxidatively induced reactivity of the complex [Fe₂(CO)₄(κ²-dmpe)(μ-adtBn)] related to the active site of [FeFe] hydrogenases. *Chem. Eur. J.* **2018**, *24*, 15036–15051. [[CrossRef](#)]
51. Farrugia, L.J. WinGX suite for small molecule single-crystal crystallography. *J. Appl. Crystallogr.* **1999**, *32*, 837–838. [[CrossRef](#)]
52. Ahlrichs, R.; Bär, M.; Häser, M.; Horn, H.; Kölmel, C. Electronic structure calculations on workstation computers: The program system Turbomole. *Chem. Phys. Lett.* **1989**, *162*, 165–169. [[CrossRef](#)]
53. Becke, A.D. Density-functional exchange-energy approximation with correct asymptotic behavior. *Phys. Rev. A At. Mol. Opt. Phys.* **1988**, *38*, 3098–3100. [[CrossRef](#)]
54. Perdew, J.P. Density-functional approximation for the correlation energy of the inhomogeneous electron gas. *Phys. Rev. B Condens. Matter Mater. Phys.* **1986**, *33*, 8822–8824. [[CrossRef](#)]
55. Schäfer, A.; Huber, C.; Ahlrichs, R. Fully optimized contracted Gaussian basis sets of triple zeta valence quality for atoms Li to Kr. *J. Chem. Phys.* **1994**, *100*, 5829–5835. [[CrossRef](#)]
56. Arrigoni, F.; Bertini, L.; Bruschi, M.; Greco, C.; De Gioia, L.; Zampella, G. H₂ Activation in [FeFe]-Hydrogenase cofactor versus diiron dithiolate models: Factors underlying the catalytic success of Nature and implications for an improved bio-mimicry. *Chem. Eur. J.* **2019**, *25*, 1227–1241. [[CrossRef](#)]

57. Basu, D.; Bailey, T.S.; Lalaoui, N.; Richers, C.P.; Woods, T.J.; Rauchfuss, T.B.; Arrigoni, F.; Zampella, G. Synthetic designs and structural investigations of biomimetic Ni–Fe thiolates. *Inorg. Chem.* **2019**, *58*, 2430–2443. [[CrossRef](#)]
58. Breglia, R.; Arrigoni, F.; Sensi, M.; Greco, C.; Fantucci, P.; De Gioia, L.; Bruschi, M. First-principles calculations on Ni,Fe-containing carbon monoxide dehydrogenases reveal key stereoelectronic features for binding and release of CO₂ to/ from the C-cluster. *Inorg. Chem.* **2021**, *60*, 387–402. [[CrossRef](#)]
59. Almazahreh, L.R.; Arrigoni, F.; Abul-Futouh, H.; El-Khateeb, M.; Görls, H.; Elleouet, C.; Schollhammer, P.; Bertini, L.; De Gioia, L.; Rudolph, M.; et al. Proton shuttle mediated by (SCH₂)₂P=O moiety in [FeFe]-hydrogenase mimics: Electrochemical and DFT studies. *ACS Catalysis* **2021**, *11*, 7080–7098. [[CrossRef](#)]
60. Eichkorn, K.; Weigend, F.; Treutler, O.; Ahlrichs, R. Auxiliary basis sets for main row atoms and transition metals and their use to approximate coulomb potentials. *Theor. Chem. Acc.* **1997**, *97*, 119–124. [[CrossRef](#)]
61. Grimme, S.; Antony, J.; Ehrlich, S.; Krieg, H. A consistent and accurate ab ini-tio parametrization of density functional dispersion correction (DFT-D) for the 94 elements H–Pu. *J. Chem. Phys.* **2010**, *132*, 154104–154122. [[CrossRef](#)] [[PubMed](#)]
62. Grimme, S.; Ehrlich, S.; Goerigk, L. Effect of the damping function in dispersion corrected density functional theory. *J. Comput. Chem.* **2011**, *32*, 1456–1465. [[CrossRef](#)] [[PubMed](#)]
63. Klamt, A. Conductor-like screening model for real solvents: A new approach to the quantitative calculation of solvation phenomena. *J. Phys. Chem.* **1995**, *99*, 2224–2235. [[CrossRef](#)]
64. Klamt, A. Calculation of UV/Vis spectra in solution. *J. Phys. Chem.* **1996**, *100*, 3349–3353. [[CrossRef](#)]